J Mater Sci (2007) 42:8700–8706
DOI 10.1007/s10853-007-1765-9

Effect of rubber particle size on the impact tensile fracture behavior of MBS resin with a bimodal particle size distribution

K. Arakawa · T. Mada · J. Takahashi ·
M. Todo · S. Ooka

Received: 16 September 2006 / Accepted: 11 April 2007 / Published online: 18 July 2007

Abstract We performed impact tensile fracture experiments on methylmethacrylate–butadiene–styrene (MBS) resin with small and large particles in a bimodal size distribution, and examined the effects of particle size on fracture behavior by fixing the total rubber content (28 wt%) and the small particle size (about 140 nm), and varying the size of large particles (about 490 nm or 670 nm). Dynamic load P' and displacement δ' of single-edge-cracked specimens were measured using a Piezo sensor and a high-speed extensometer, respectively. A P'–δ' diagram was used to determine external work U_{ex} applied to the specimen, elastic energy E_e stored in the specimen, and fracture energy E_f for creating a new fracture surface A_s. Energy release rate was then estimated using $G_f = E_f/A_s$. Values of G_f were correlated with fracture loads and mean crack velocity v_m determined from load and time relationships. We then examined the effect of particle size on G_f and v_m, and results indicated that particle size plays an important role in changing the values of G_f and v_m.

K. Arakawa (✉) · T. Mada · M. Todo
Research Institute for Applied Mechanics, Kyushu University,
6-1 Kasuga-koen, Kasuga 816-8580, Japan
e-mail: k.arakaw@riam.kyushu-u.ac.jp

J. Takahashi
Interdisciplinary Graduate School of Engineering Sciences,
Kyushu University, 6-1 Kasuga-koen, Kasuga 816-8580, Japan

S. Ooka
Denki Kagaku Kogyo, Polymer Research Center, Chiba Plant,
Ichihara 290-8588, Japan

Introduction

Particle dispersion methods have been widely applied on many types of materials to improve their mechanical reliability. For example, brittle polymers exhibit increased impact resistance when rubber particles are dispersed in resin matrix. This method has been used on materials including high impact strength polystyrene (HIPS) and acrylonitrile–butadiene–styrene (ABS) resin, and studies have verified its validity and applicability. The mechanisms of fracture behavior in these materials have also been investigated from micro- and macroscopic perspectives. Rubber particles reportedly play an important role in enhancing impact resistance by generating crazes, shear bands, and cavitations around particles near a crack front in the material [1–3]. The same method has been employed to increase impact resistance in a transparent polymer, methylmethacrylate–butadiene–styrene (MBS) resin [4–7]. However, rubber particles in the resin deteriorate important material properties such as transparency and rigidity or modulus. Therefore, it is critically important to design and optimize the size of rubber particles, total rubber content, and the refractive index of the particles. Recent studies have investigated the effect of a bimodal distribution of rubber particle sizes and its validity and applicability [4–7]. Takahashi et al. [5, 6] studied this problem using two kinds of MBS resins and reported that the bimodal distribution improves not only the falling weight impact strength but also the transparency of the resin. They also suggested that the bimodal particle size plays an important role in generating microscopic shear bands and cavitations around and between the small and large particles near a crack front under the impact loading [5, 6].

We examined the fracture behavior of MBS resin with a bimodal rubber particle size distribution. To examine the effects of particle size, the total rubber content (28 wt%) and the size of small particles (about 140 nm) were unchanged and the size of large particles were either about 490 nm or 670 nm. Single-edge-cracked tensile specimens were fractured under impact tensile loading, and impact load and specimen displacement were measured using a Piezo sensor [8] and high-speed extensometer [9], respectively, to evaluate external work U_{ex} applied to the specimen. Elastic energy E_e and nonelastic energy E_n were estimated from the oscillation of the split specimen just after fracture. Fracture energy E_f was then determined and correlated with fracture load P_c. For fracture surface A_s, the energy release rate was evaluated using $G_f = E_f/A_s$. Mean crack velocity v_m was also estimated as a function of P_c. This paper presents the results and discusses the effects of large particle sizes.

Specimen material

Experiments were conducted on MBS resin with a bimodal rubber particle size distribution provided by Denki Kagaku Kogyo. Figure 1 shows the resin microstructure, and Table 1 lists the average rubber particle diameters and weight fractions. The resin matrix was the copolymer of methylmethacrylate–styrene, and rubber particles were prepared by a graft polymerization of styrene monomer and (meth)acrylate monomer on styrene–butadiene rubber. Large rubber particles were prepared by carrying out bulk polymerization of the monomers in dissolved styrene–butadiene rubber (rubber content 10 wt%) by stirring, while small rubber particles were prepared by performing emulsion polymerization of the monomers in a latex of styrene–butadiene rubber (rubber content 70 wt%) [5].

In this experiment, total rubber content (28 wt%) and small particle size (about 140 nm) were unchanged, but the size of large particles was either about 490 nm or 670 nm.

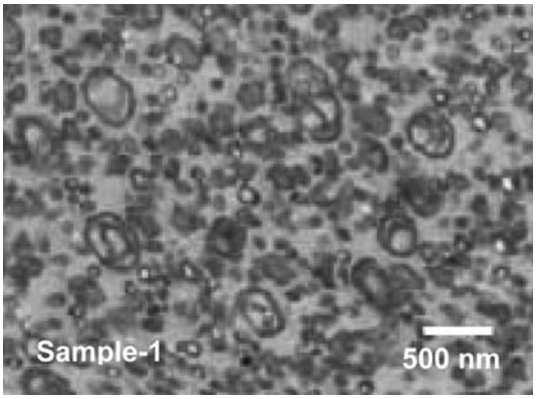

Fig. 1 Microstructure of MBS resin (Sample-1)

Table 1 Weight fractions of rubber particles in MBS resin

	Large particle		Small particle
Diameter (nm)	490	670	140
Sample-1 (wt%)	70	0	30
Sample-2 (wt%)	0	70	30

The composition of rubber/poly(meth)acrylate/polystyrene was 28/31/41, the average molecular weight was 150,000, the melt flow index under 200 °C and 5 kg was 1.5 g per 10 min, and the glass transition temperature was about 90 °C. The dumbbell-type specimens were injection-molded from pellets after melting extrusion. When large particle size increased, transparency of the specimen deteriorated slightly because the larger particles affected surface flatness. However, no changes were observed in their static material properties. The yield stress, fracture stress and strain under tensile loading were 34 MPa, 25 MPa and 40%, respectively. This suggests that total rubber content is an influential parameter in determining the static properties. No big difference was also observed on the dispersion of the particles between the pellets and specimens since the particles with cross-linked structure were not deformed significantly during the injection-molding. Figure 2(a) illustrates the specimen geometry. To change the fracture initiation load of specimens or external work applied to the specimen, sharp pre-cracks with lengths varying from about 1–4.5 mm were generated by forcing a razor blade into a pre-machined saw-cut on the specimen's edge. By varying this distance, values of the mean crack velocity in the specimens were also varied.

Experimental methods

An impact tensile load was introduced using a special loading device that utilizes the free-fall of a weight [8]. As illustrated in Fig. 2(b), this device consists of an electromagnet that holds the weight at an arbitrary height, a metal frame for converting the impulse force into tension, loading axes for mounting the specimen, and a Piezo sensor for measuring the impact load. The specimen was clamped rigidly at its lower and upper parts to satisfy the requirements for specimen symmetry. A 3–mm-thick rubber sheet was mounted on the upper end of the frame to attenuate high-frequency vibrations caused by the impact.

All specimens were loaded by dropping a 10-kg weight from a height of 300 mm, so that the impact velocity of the weight was about 2.4 m/s. The sensor had a frequency response of 45 kHz, so it permitted dynamic measurements [8]. Load P applied to each specimen was partitioned into an initial static load P_o due to the metal frame's dead

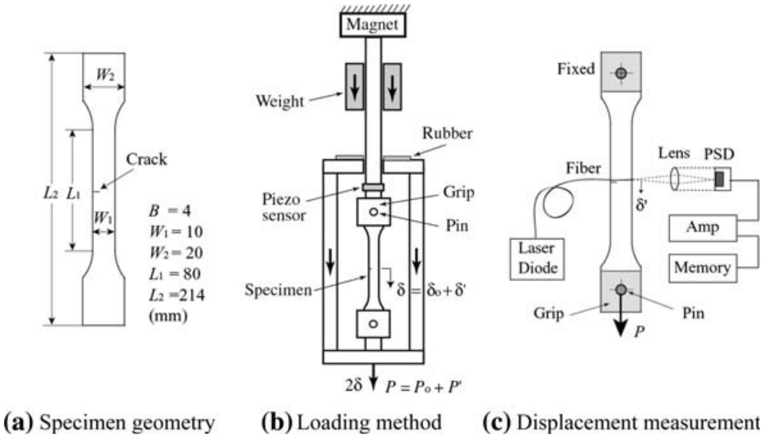

(a) Specimen geometry (b) Loading method (c) Displacement measurement

Fig. 2 Specimen geometry and experimental setup for loading and displacement measurement (**a**) Specimen geometry, (**b**) Loading method, (**c**) Displacement measurement

weight, and a dynamic load P' due to the impact (see Fig. 2(b)). Tests were conducted at room temperature, and deformation of the loading axis was disregarded because it was much stiffer than the specimen. Displacement δ at the specimen's centerline was also evaluated and partitioned into an initial static value δ_o and a dynamic value δ'.

Figure 2(c) illustrates the configuration for displacement measurement using an optical fiber and a position-sensing detector (PSD) (SiTek Electro Optics). In this experiment, the fiber was attached to the upper region at a point 2 mm from the pre-crack to avoid damage caused by dynamic crack propagation. However, this influence on dynamic displacement δ' was disregarded because measurements were likely only a few percent smaller than they would have been at the specimen's centerline. A laser diode was used as a light source, and an amplifier and digital wave memory were used to record output signals from the PDS. The PSD is an optoelectronic device that converts an incident light spot into continuous position data using the lateral photo effect, and it has a frequency response of 100 kHz, so it permitted both static and dynamic displacement measurements [9].

Definition of fracture energy

Figure 3 plots load P versus displacement δ for the frame's dead weight (see Fig. 2(b)). In this figure, P_o and δ_o indicate initial static values due to the dead weight, and P_c and δ_c denote critical dynamic values at the onset of fracture. Although P–δ relationships generally differ between static and dynamic loads, this analysis assumed they were identical for simplicity. External work U_{ex} applied to half the specimen is then given as

$$U_{ex} = \frac{P_c \delta_c}{2} = \frac{\delta'_c (P_o + P'_c)^2}{2P'_c}, \qquad (1)$$

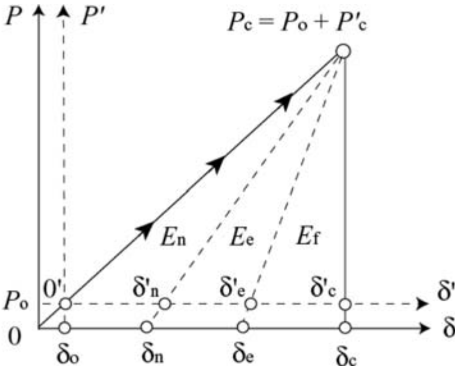

Fig. 3 Load P versus displacement δ diagram for a specimen with initial load P_o

where $P_c = P_o + P'_c$ and $\delta_c = \delta_c{}' P_c/P_c{}'$. Equation (1) is valid when P_o and δ_o are much smaller than P_c and δ_c, and nonlinearity due to the material's viscoelastic and plastic deformation during impact is not significant.

This analysis also assumed that U_{ex} can be partitioned into three regions, as shown in Fig. 3 [10, 11]:

$$U_{ex} = E_f + E_e + E_n, \qquad (2)$$

where E_f is the fracture energy created for half the new surfaces $2A_s$ which includes the energy loss due to the generation of microscopic shear bands and cavitations near the surfaces, E_e is the specimen's elastic energy, and E_n is the nonelastic energy of the specimen material due to the viscoelastic and plastic deformation [10, 11].

E_e and E_n were determined under the following assumptions. First, E_e was converted into the kinetic energy of the split specimen after fracture. Then, the material's viscosity could be neglected during dynamic crack propagation [12], so the change from P_c to δ_e or δ_n was elastic (see Fig. 3). Finally, the following relationships held:

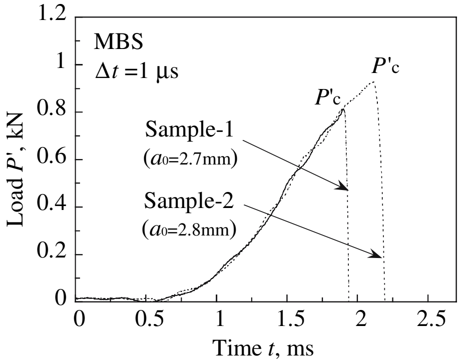

Fig. 4 Dynamic load P' as a function of time t (sampling time $\Delta t = 1$ µs)

$$\frac{E_e}{U_{ex}} = \frac{(\delta_e - \delta_n)}{\delta_c}, \frac{E_n}{U_{ex}} = \frac{\delta_n}{\delta_c}. \quad (3)$$

Results and discussion

Dynamic load P' and displacement δ'

The Piezo sensor was used to measure the dynamic load P' applied to the specimen (see Fig. 2(b)). Figure 4 plots the value of P' as a function of time t, showing experimental results of two samples with almost identical initial crack lengths. P' increased with t, and then fell abruptly from P_c' as the crack started to propagate. Note that sample-2 yielded much greater P_c' values than sample-1.

In this experiment, fracture load P_c' was determined from six specimens of each sample. The results obtained from single tests were plotted in Fig. 5 as a function of the initial crack length a_0. P_c' decreased with a_0, but sample-2 yielded greater P_c' values than sample-1 for a given a_0, suggesting that fracture behavior could be changed by increasing the size of large particles from about 490 to about 670 nm even when the rubber content is identical.

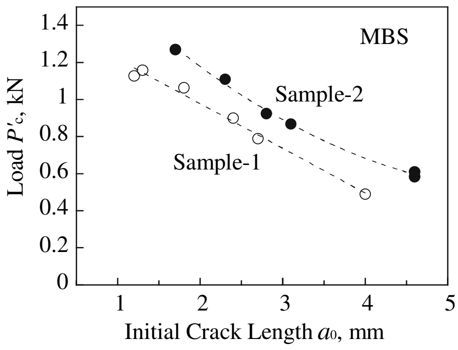

Fig. 5 Fracture load P_c' versus initial crack length a_0

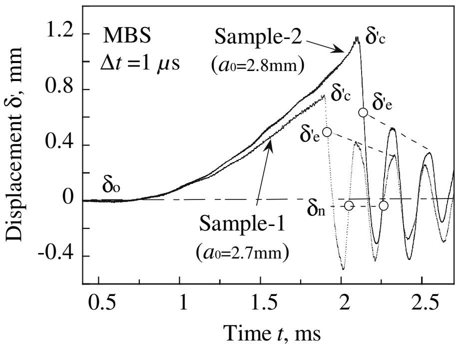

Fig. 6 Dynamic displacement δ' as a function of time t (sampling time $\Delta t = 1$ µs)

Figure 6 illustrates dynamic displacement δ' measured using the optical fiber and PSD (see Fig. 2(c)). As shown in the figure, δ' increased with time t, and then fell abruptly as the fracture initiated at the critical value δ_c'. After fracture, δ' exhibited damping oscillation. Note that sample-2 yielded greater δ_c' values than sample-1, similar to findings for fracture load P_c' (see Fig. 4).

Figure 7 plots the variation in critical displacement δ_c' versus load P_c'. δ_c' increased with P_c', suggesting they had a linear relationship, and sample-2 yielded greater δ_c' values than sample-1 for a given P_c'. This implies that the large particles can increase specimen elongation to fracture under impact different from the static loading conditions.

External work U_{ex}

Figure 8 illustrates the relationship between dynamic load P' and displacement δ' for sample-1 determined from Figs. 4 and 6. Although a slight change appeared in the P'–δ' diagram, we assumed a linear relationship between P' and δ', as shown in Fig. 3. Since the conditions were the same for sample-2, external work U_{ex} was evaluated using Eq. (1). In Fig. 8, the dynamic external work U_{ex}' is partitioned into two regions of the elastic energy E_e' and

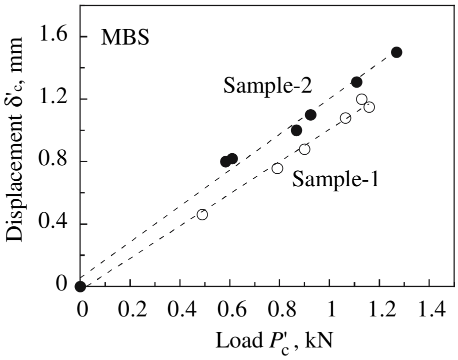

Fig. 7 Critical displacement δ_c' as a function of fracture load P_c'

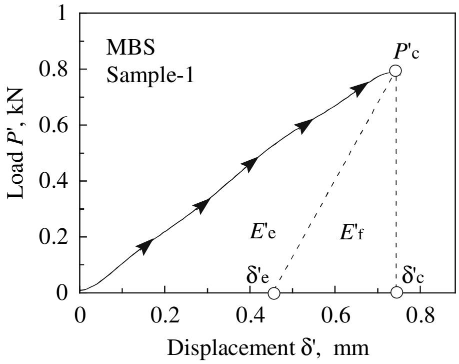

Fig. 8 The relationship between dynamic load P' and displacement δ'

fracture energy E_f', and the nonelastic energy E_n' is disregarded. The reason for this will be discussed later.

Figure 9 plots the variations in external work U_{ex} versus load P_c (=$P_o + P_c'$). As the figure illustrates, U_{ex} increased with P_c, indicating that sample-2 had a greater U_{ex} value than sample-1 for a given P_c. This suggests that changing the size of large particles can increase fracture energy.

Elastic energy E_e

The elastic displacement δ_e must be determined to evaluate a specimen's elastic energy E_e (see Fig. 3). This was achieved by measuring displacement δ' beside the crack position before and after fracture (see Fig. 2(c)). As shown in Fig. 6, δ' dropped abruptly as the fracture initiated at the critical value δ_c', and then exhibited damping oscillation after fracture. If there was a noticeable amount of nonelastic deformation in the specimen, the centerline of the oscillation should be larger than the initial static displacement δ_o (=0.05 mm). However, δ' oscillated around δ_n, which was smaller than δ_o, suggesting that no great residual displacement was caused by viscoelastic or plastic deformation. This result was typical of impact tensile fracture behavior among specimens. Hence, we could disregard nonelastic energy E_n in Eqs. (2) and (3). We also attributed the damping oscillation in Fig. 6 to energy loss caused by elastic wave propagation in the specimen's loading axes.

The energy ratio E_e/U_{ex} in Eq. (3) was calculated as follows. First, amplitudes of the initial two oscillations were measured to estimate their attenuation (see Fig. 6). This attenuation was used to determine the intersection with falling curve δ', i.e., dynamic value δ_e' just after fracture. Finally, δ_e was determined using the following relationship (see Fig. 3):

$$\delta_e = \frac{\delta_e'(P_o + P_c')}{P_c'}. \tag{4}$$

Figures 10 and 11 plot E_e/U_{ex} as a function of P_c. The E_e/U_{ex} of sample-1 decreased from 61% to 50% when P_c increased, while that of sample-2 increased slightly from 38% to 45%. The cause for this is not clear, but might be related to the dynamic behavior of crack propagation in the two samples.

Fracture energy E_f

Figures 10 and 11 also show the energy ratio E_f/U_{ex} derived from Eq. (2) by assuming $E_n = 0$. The E_f/U_{ex} for sample-1 increased with P_c, while that for sample-2 decreased. Sample-1 yielded about 39% in the region of small P_c and about 50% in the region of large P_c, and corresponding values for sample-2 were about 62% and 55%. This suggests that the fracture load and size of large particles can change fracture energy.

Energy release rate G_f

Energy release rate G_f was estimated using the following equation:

$$G_f = E_f/A_s, \tag{5}$$

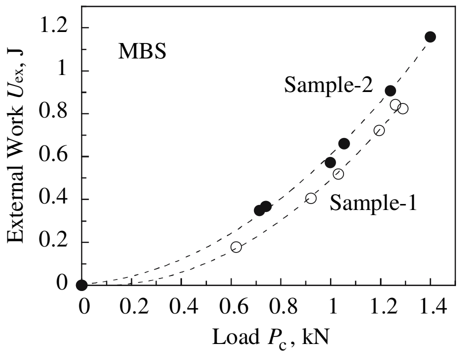

Fig. 9 External work U_{ex} as a function of fracture load P_c

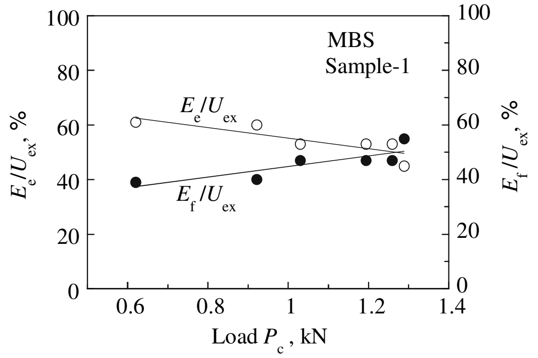

Fig. 10 Energy ratios E_e/U_{ex} and E_f/U_{ex} as a function of fracture load P_c (Sample-1)

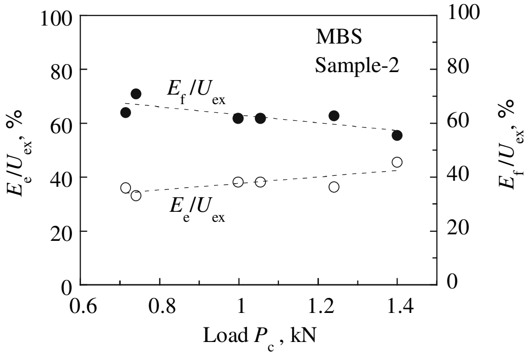

Fig. 11 Energy ratios E_e/U_{ex} and E_f/U_{ex} as a function of fracture load P_c (Sample-2)

where A_s is half the area of the total fracture surface. Figure 12 shows G_f values as a function of P_c. G_f for both samples increased with P_c, and sample-2 yielded much greater G_f values than sample-1 for a given P_c. This indicates that the rate of energy release increases with fracture load and is influenced by a sample's microstructures.

To determine why G_f increased with P_c and changed with particle size, we evaluated the mean crack velocity v_m in each specimen. This was achieved by measuring fall time Δt from P_c' to $P = 0$ in the P'–t diagrams. Samples-1 and -2 in Fig. 4 had Δt values of about 38 µs and 89 µs, respectively, and the corresponding v_m values were about 190 m/s and 81 m/s.

Figure 13 plots mean crack velocity v_m as a function of fracture load P_c. Several interesting findings appeared in their relationships. First, v_m increased with P_c, similar to findings for energy release rate G_f (see Fig. 12). Second, v_m values for the two samples were quite different: sample-1 yielded v_m values greater than 150 m/s, while values for sample-2 were less than 100 m/s. Finally, an opposite relationship appeared between G_f and v_m: sample-1 yielded high v_m and low G_f values, while sample-2 yielded low v_m and high G_f values. The cause of this is not clear, but might be related to crack extension resistance from large particles since the two samples had the same total rubber content. The corresponding fracture surfaces of specimens tended to become rougher as G_f and v_m increased, implying that the energy consumed creating a fracture surface increases as the crack propagates at higher values of G_f and v_m.

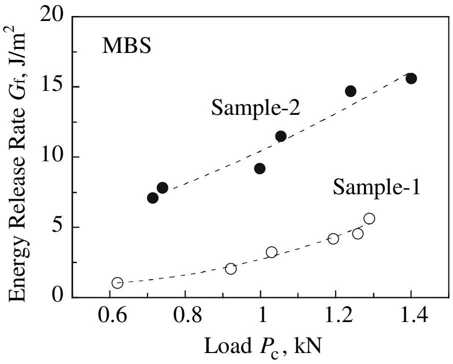

Fig. 12 Energy release rate G_f as a function of fracture load P_c

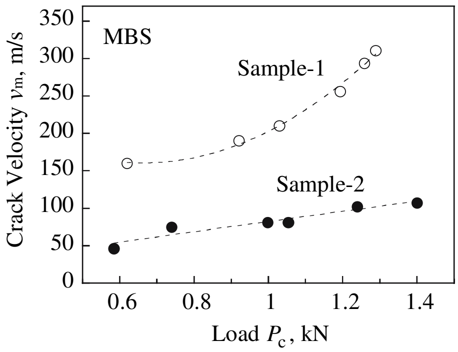

Fig. 13 Mean crack velocity v_m as a function of fracture load P_c

Conclusions

We used an impact tensile device and an optical high-speed extensometer to examine brittle fractures of MBS resin with a bimodal rubber particle size distribution, and measured the impact load and displacement of single-edge-cracked specimens to determine the external work U_{ex} applied to the specimen. We estimated the elastic energy E_e and nonelastic energy E_n just after fracture based on the oscillation of the split specimen. Fracture energy E_f was then determined and correlated with fracture load P_c. The energy release rate was evaluated with fracture surface A_s using $G_f = E_f/A_s$, and the mean crack velocity v_m was also estimated from the load-time diagram. In this experiment, total rubber content (28 wt%) and the size of small particles (about 140 nm) were unchanged, and the size of large particles were either about 490 nm or 670 nm. The following results were obtained.

(1) Nonelastic energy E_n can be disregarded under the impact tensile loading conditions tested.
(2) Fracture load P_c, displacement δ_c, and external work U_{ex} increased when the size of large particles increased from about 490 nm to 670 nm for a given initial crack length.
(3) Energy release rate G_f and mean crack velocity v_m increased with P_c.
(4) The sample with the largest particle size (about 670 nm) yielded higher G_f values but lower v_m values for the same total rubber content.

References

1. Kambour RP, Rusell RR (1971) Polymer 12:237
2. Keskkula H, Schwarz M, Paul DR (1986) Polymer 27:211
3. Michler GH (1986) Polymer 27:323
4. Tkahashi J, Watanabe H, Nakamoto J, Ito T (2002) Kobunshi Ronbunshu 59(9):527 (in Japanese)
5. Tkahashi J, Watanabe H, Nakamoto J, Ito T (2003) Kobunshi Ronbunshu 60(1):6 (in Japanese)
6. Tkahashi J, Watanabe H, Nakamoto J (2004) Kobunshi Ronbunshu 61(2):114 (in Japanese)
7. Tkahashi J, Watanabe H, Nakamoto J, Arakawa K, Todo M (2006) Polymer J 38(8):835
8. Takahashi K, Mada T, Beguelin P (1998) Trans Jpn Soc Mech Eng Ser A 64(628):2975 (in Japanese)
9. Mada T, Tkahashi K, Beguelin P, Aggag G (1997) Trans Jpn Soc Mech Eng Ser A 63(611):1431 (in Japanese)
10. Arakawa K, Mada T (2004) Trans Jpn Soc Mech Eng Ser A 70(695):936 (in Japanese)
11. Arakawa K, Mada T (2006) Exp Mech 46:347
12. Arakawa K, Nagoh D, Takahashi K (1999) Inter J Fracture 96:347